Progress In Electromagnetics Research, Vol. 138, 307–325, 2013

ESTIMATION OF POSE ANGLE FOR TRIHEDRAL IN ULTRAWIDEBAND VIRTUAL APERTURE RADAR

Bo Chen, Tian Jin*, Zhimin Zhou, and Biying Lu

College of Electronic Science and Engineering, National University of Defense Technology, Changsha, Hunan 410073, China

Abstract—A map of a building using through-the-wall radar imaging (TWRI) can be best obtained by detecting and identifying its internal principal scatterers, where estimation of the pose angle of a trihedral formed by the wall-wall-floor structure is important in this application. In this paper, an image-domain based method is proposed to estimate the pose angle of trihedral using a feature called *amplitude ratio* (AR). The estimated pose angle of a trihedral is determined according to AR. Firstly, the imaging geometry of the radar with a multiple-input multiple-output (MIMO) array and the definition of AR in the echo-domain are described. Secondly, a parametric back-scattering model based on geometrical theory of diffraction (GTD) is applied to analyze AR in the echo-domain when a trihedral is in different pose angles. Thirdly, a virtual aperture imaging model is developed to describe the imaging procedure using MIMO array. Based on the imaging model, the AR of each trihedral can be calculated in the image-domain instead of the echo-domain. Finally, the proposed estimation method is validated by the real data collected in an anechoic chamber.

1. INTRODUCTION

The technology of sensing through walls has received considerable attention in recent years. Electromagnetic waves are provided with the ability of penetrating man-made building materials and imaging targets behind opaque structures. As a result, through-the-wall radar imaging (TWRI) is considered very effective to achieve the objectives of "seeing" through walls using electromagnetic waves [1]. TWRI is highly desirable for a range of organizations, including police, fire and rescue personnel missions, surveillance, first responders, and defense forces [2–5].

Received 5 December 2012, Accepted 11 March 2013, Scheduled 26 March 2013

* Corresponding author: Tian Jin (tianjin@nudt.edu.cn).

Most through-the-wall radars in use often require a close position to the wall or they have to be pressed against the wall [6–9]. Moreover, TWRI mainly focuses on behind-the-wall target [10–15]. Nowadays, mapping the layout of the building is demanded. Such systems will greatly improve security, response time, covertness, and reliability of these tasks [16–19].

In literatures, there is consensus on the fact that a map of a building can be best obtained by detecting and identifying principal scatterers inside a building, i.e., corners, planar walls, etc. Therefore, plate, dihedral and trihedral consist of the dominating principal scatterers in a building. The procedure of mapping a building is shown in Fig. 1. The classifier divides the scatterers appeared in the radar image into three types of principal scatterers as aforementioned. The estimator determines the pose angle of each scatterer. The layouts of a building will be obtained after we use the classifier and the estimator.

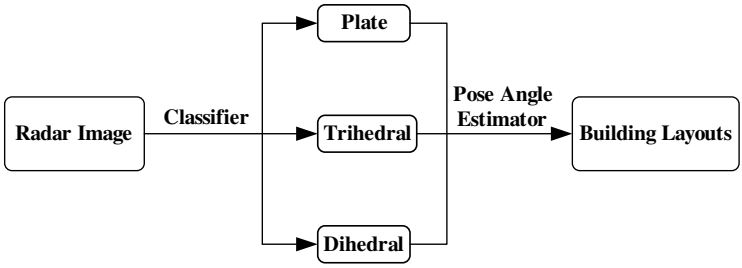

Figure 1. Procedure of mapping the layouts of a building.

However, the views on the best way to identifying principal scatterers differ greatly [16]. Attributed Scattering Center Model (ASCM) is considered to be an effective way to identifying principal scatterers such as sphere, plate, dihedral and trihedral, etc. [20]. This model describes the relationship between the back-scattering field and frequency as well as the aspect-angle. In addition, polarimetric feature supplies another way to identify radar targets. Space-frequency domain instantaneous polarization characteristics of principal scatterers are researched and applied on target classification and geometrical structure retrieval [21].

The above research are appreciable in promoting principal scatterers classification. But these methods are incapable of estimating the pose angles of those canonical scatterers. Meanwhile, the layout of a building can be more accurately determined if we have known the pose angle of each principal scatterer according to Fig. 1. Moreover, pose angles of the plates and the dihedra inside a building are easily

known if we have obtained the pose angles of the interior trihedra. This paper intends to develop an effective method to estimate the pose angle of the trihedral. Conventionally, we can get the pose angle of a trihedral in the echo-domain by probing into the amplitude ratio (AR) variety which is a function of the pose angle. The definition of AR will be given in Section 2. The echo-domain based method has a limitation that it is constrained to process echo from only one trihedral. However, there are often more than one trihedral inside a building. As a result, the echo-domain based method is not suitable for mapping the building interior structure. In this paper, we have proposed an effective pose angle estimation method from the image formed by a virtual aperture. The virtual aperture can be obtained by a multiple-input multiple-output (MIMO) array, which is widely used in TWRI. A virtual aperture imaging model is developed, based on which the AR is calculated in the image-domain instead of the echo-domain to deal with the case of multiple trihedra. Moreover, we have collected experimental data to validate the effectiveness of the proposed image-domain based method.

The remainder of this paper is organized as follows. A MIMO array imaging geometry for TWRI and the definition of AR is given in Section 2. Section 3 presents a parametric back-scattering model for trihedral to build the relationship between AR and pose angle in the echo-domain. After clarifying the constraints of calculating AR in the echo-domain, Section 4 proposes an image-domain based method to obtain AR by using a virtual aperture imaging model. In Section 5, real data are collected in the anechoic chamber to validate the proposed method. Finally, some concluding remarks are drawn in Section 6.

2. MIMO IMAGING GEOMETRY AND DEFINITION OF AR

2.1. Imaging Geometry of MIMO Array

TWRI can obtain the high-resolution imagery of buildings, which offers valuable information for target discrimination or recognition. There has been significant amount of study on TWRI. Most existing TWRI systems are synthetic aperture radar or real aperture radar systems. The TWRI with synthetic aperture makes the antenna moving along a rail to form the aperture [22]. The scattered electromagnetic field is being spatially sampled in a dense regular grid, which makes data acquisition too slow. The TWRI with real aperture uses an array with each element being a transceiver. The TWRI with real aperture can collect a whole aperture data in the order of millisecond to ensure the capability of continuous imaging. This is very useful in behind-the-

wall motion target detection. The main drawback of a real aperture system is the heavier-weight and higher-cost compared with a synthetic aperture system.

In recent years, MIMO radars have attracted great interest [23–28]. In large part, this interest stems from the enormous potential for MIMO techniques to yield lighter-weight, lower-cost systems as compared with the conventional phased arrays of comparable performance. The MIMO array with M transmitting elements and N receiving elements can obtain a virtual aperture with $M \times N$ virtual transceivers, which reduces the weight and cost greatly. Therefore, the virtual aperture is more suitable to TWRI systems than the real or synthetic aperture.

A MIMO array can be regarded as the combination of several single-input and multiple-output (SIMO) arrays. Thus, we will develop the imaging model based on SIMO array at first.

The back-projection (BP) algorithm is a time-domain image formation [29], whose basic idea is to coherently sum the echo according to the time delay calculated on the imaging geometry. BP is widely used in TWRI. Assuming r and y represents the range and cross-range, respectively. $I_m(r, y)$ is the image of the mth SIMO array. Employing its basic idea, a modified BP algorithm to form $I_m(r, y)$ according to the imaging geometry of the SIMO array with N receiving elements is

$$I_m(r,y) = \sum_{n=1}^{N} \left[\int s_m(t,n)\delta\left(t - \frac{\sqrt{r^2+(y-y_{Tm})^2}+\sqrt{r^2+(y-y_{Rm})^2}}{c}\right)dt \right] \quad (1)$$

where c is the speed of light, $\delta(\cdot)$ the Dirac impulse function, t the fast-time, and $s_m(t, n)$ the received echo of the mth SIMO array with the mth transmitting element (Tx) and nth receiving element (Rx) located at $(0, y_{Tm})$ and $(0, y_{Rm})$, respectively.

Figure 2 illustrates the SIMO imaging geometry. The receiving elements are divided into the left half part and the right half part which will be useful in defining the AR subsequently. We define $K = [N/2] + 1$, where $[N/2]$ represents the nearest integer which is less than $N/2$. If N is an odd number, the left half is $n = 1, 2, \ldots, K$, and the right half is $n = K, K+1, \ldots, N$. If N is an even number, the left half is $n = 1, 2, \ldots, K$, and the right half is $n = K + 1, \ldots, N$. In the following figure, N is treated as an even number to illustrate the estimation algorithm for convenience. θ_T and θ_R denote the aspect-angles of the Tx and Rx elements with respect to the target, respectively. θ_R^n $(n = 1, 2, \ldots, N)$ represents the aspect-angle of the nth Rx element.

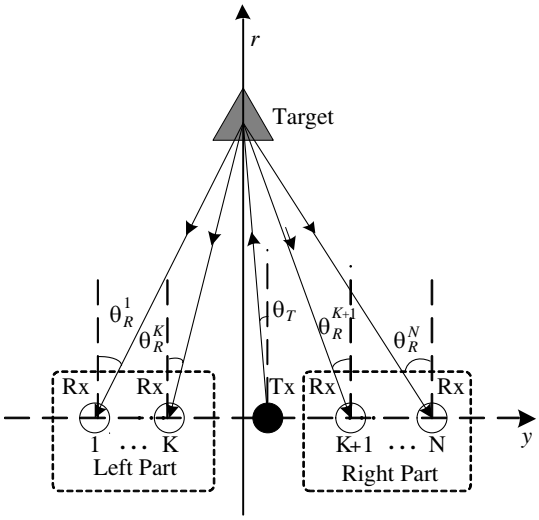

Figure 2. Imaging geometry of a SIMO array.

2.2. Definition of AR

We have known that some principal scatterers such as sphere and tophat are symmetric in cross-range direction. Namely, if θ_T is fixed, the ratio of echo intensity from the left part receiving elements to those from the right part receiving elements will be invariable even when the pose angle θ_P of the sphere or tophat varies. However, the above symmetric feature is inapplicable for trihedral. The ratio will varies with θ_P.

Before we give the definition of AR, a coordinate system for trihedral is established as is shown in Fig. 3. The pose angle is defined as the rotation angle from x-axis OX to the diagonal of the square plate OA. $\theta_P > 0$ means anti-clockwise rotation and $\theta_P < 0$ means clockwise rotation. Thus, the trihedral illustrated in solid line and dashed line represent the pose angle of the trihedral equals 0° and θ_P, respectively.

As a result, AR is the function of the pose angle of trihedral θ_P, and the incident angle θ_T is an important parameter in developing the estimation method. Assuming that f is the frequency, f_L and f_H denote the lowest and highest operating frequencies, respectively.

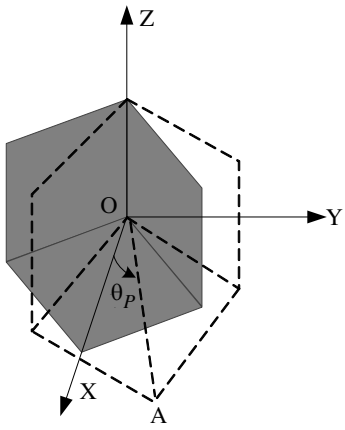

Figure 3. Coordinate system for trihedral.

$\rho(\theta_P;\, \theta_T)$ represents AR which is defined in the echo-domain as follows:

$$\rho(\theta_P;\theta_T) = \frac{\sum\limits_{n=1}^{K} \int_{f_L}^{f_H} |FT_{t\leftrightarrow f}\left[s(t,n)\right]|\, df}{\sum\limits_{n=K+1}^{N} \int_{f_L}^{f_H} |FT_{t\leftrightarrow f}\left[s(t,n)\right]|\, df} \triangleq \frac{A_L}{A_R} \tag{2}$$

where $FT_{t\leftrightarrow f}[\cdot]$ is Fourier transform (FT) with respect to t. A_L and A_R are defined as echo intensity from the left part receiving elements and the right part receiving elements, respectively. From Equation (2), it can be inferred that we will get the estimated pose angle $\hat{\theta}_P$ if the function $\rho(\theta_P;\, \theta_T)$ and the calculated AR are known.

3. CALCULATION OF AR IN THE ECHO-DOMAIN

3.1. Parametric Back-scattering Model for Trihedral

In this section, a parametric back-scattering model is used to determine the AR $\rho(\theta_P;\, \theta_T)$ in the echo-domain according to Equation (2) when a trihedral is in different pose angles.

The parametric models for the frequency and angle dependence of the principal scatterers are available in the literature [30]. However, these models are suitable for monostatic radar. To estimate the pose angle of a trihedral when radar operates in MIMO array measurement configuration, we make use of parametric models of canonical shapes for bistatic radar. Geometric theory of diffraction (GTD) solutions

is generalized for scattering mechanisms in a plane to develop three-dimensional models for six canonical shapes: rectangular plate, dihedral, trihedral, cylinder, top-hat, and sphere [31]. The proposed models provide physically relevant yet compact scattering solutions that are easily implemented for radar signal processing and automatic target recognition (ATR) applications.

We denote β_T and β_R as the elevation angle of the transmitter and receiver with respect to the target. According to the literature, the square trihedral peak scattering occurs at $\beta_T = \beta_R = \tan^{-1}(1/\sqrt{2}) \triangleq \beta_0$, not at $\beta = 45°$. The trihedral scattering response is modeled as [31]

$$\begin{aligned} M_{tri}(\Theta_{tri}) = & \frac{jkA}{2\sqrt{\pi}}\text{sinc}[kH(\cos\beta_T - \cos\beta_R)] \\ & \times \left[\text{sinc}\left[kH\left(\cos\left(\theta_R - \frac{\pi}{4}\right)\cos\beta_R - \cos\left(\theta_T - \frac{\pi}{4}\right)\cos\beta_T\right)\right]\right. \\ & \left. + \text{sinc}\left[kH\left(\cos\left(\theta_R + \frac{\pi}{4}\right)\cos\beta_R - \cos\left(\theta_T + \frac{\pi}{4}\right)\cos\beta_T\right)\right]\right] \\ & \times \left\{ \begin{array}{ll} \sin\left(\dfrac{\beta_T + \beta_R}{2} + \dfrac{\pi}{4} - \beta_0\right), & \beta_R \in [0, \beta_0] \\ \cos\left(\dfrac{\beta_T + \beta_R}{2} + \dfrac{\pi}{4} - \beta_0\right), & \beta_R \in \left[\beta_0, \dfrac{\pi}{2}\right] \end{array} \right\} \\ & \times \left\{ \begin{array}{ll} -\cos\left(\dfrac{\theta_T + \theta_R}{2} - \dfrac{\pi}{4}\right), & \theta_R \in \left[-\dfrac{\pi}{4}, 0\right] \\ \sin\left(\dfrac{\theta_T + \theta_R}{2} - \dfrac{\pi}{4}\right), & \theta_R \in \left[0, \dfrac{\pi}{4}\right] \end{array} \right\} \end{aligned} \tag{3}$$

where the length of the trihedral along each edge is assumed to be equal to H and $A = 2\sqrt{3}H^2$. k represents the wavenumber. β_T and β_R are assumed to be equal in general. AR is relevant to θ_T and θ_R. Moreover, θ_R is relevant to the pose angle θ_P according to the coordinate system established in Fig. 3. Therefore, using the above parametric model, the AR variety characteristics can be directly obtained in the echo-domain.

3.2. Limitation of Calculating AR in the Echo-domain

The definition of AR provides us a direct way to estimate the pose angle of a trihedral in the echo-domain. If we have got the value of AR, we choose the pose angle whose corresponding AR equals the calculated AR as the estimated result. However, this echo-domain based method is constrained to process echo data from only one trihedral. This is unpractical for processing field data due to the existence of more than one trihedral inside a real building, even the building is made up of

only four walls. Next, we will develop an effective pose angle estimation method by utilizing a virtual aperture imaging model to compute AR in the image-domain instead of the echo-domain. With the capability of determining the pose angles of all the trihedra appearing in an image, it has overcome the constraints of the echo-domain method.

4. CALCULATION OF AR IN THE IMAGE-DOMAIN

4.1. Separating Multiple Trihedrals

As mentioned above, echo-domain method has a limitation constrained to process echo data from only one trihedral. But in a man-made building, there are often many trihedra. Consequently, the echo-domain based method is of no effect. We will develop an image-domain based method to estimate the pose angle of trihedral by using a virtual aperture method. The outline of the method is illustrated in Fig. 4.

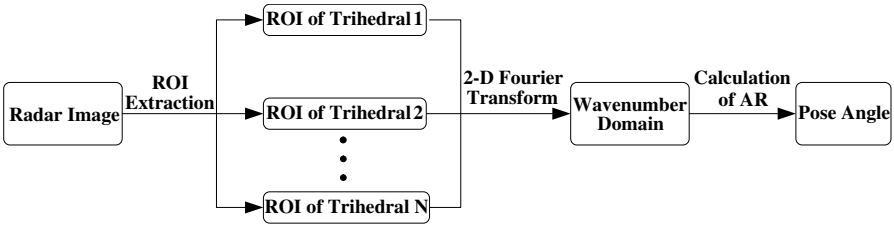

Figure 4. Estimating the pose angles of multiple trihedra in the image-domain.

4.2. Virtual Aperture Imaging Model

The BP algorithm shown in Equation (1) is often used for TWRI when radar operates in MIMO array configuration. Radar image quality can be measured in terms of the Fourier Transform of point spread function (PSF), which occupies a certain area in the wavenumber domain and is denoted as region of support (ROS). The size of the ROS determines the image resolution, and the shape of the ROS determines the direction of sidelobes. Now we will describe how to acquire the left part intensity and the right part intensity based on ROS.

Figure 5(a) shows the propagation procedure of the incident electromagnetic wave transmitted by a Tx element to the target and the target's scattered electromagnetic wave received by a Rx element, which can be regarded to exist a virtual element to transmit electromagnetic wave and receive the scattered echo with θ_V being

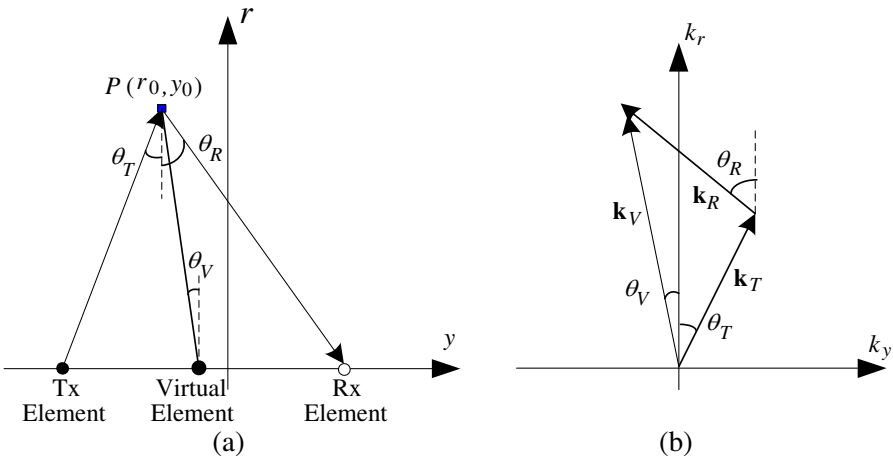

Figure 5. Virtual element imaging geometry. (a) Space domain, (b) wavenumber domain.

the aspect-angles of the virtual element with respect to the target. Therefore, each Tx-Rx pair can obtain a virtual element [32]. The propagation procedure of electromagnetic wave in the space domain can also be represented in the wavenumber domain as depicted in Fig. 5(b), where $\mathbf{k}_T$, $\mathbf{k}_R$, and $\mathbf{k}_V$ are the transmitting wavenumber, the receiving wavenumber, and the virtual wavenumber, respectively. r_0 and y_0 represent the range and the cross-range location of the target, respectively.

Moreover, the transmitting wavenumber $\mathbf{k}_T$ and the receiving wavenumber $\mathbf{k}_R$ can be expressed as follows:

$$\begin{cases} \mathbf{k}_T = k_T \cos\theta_T \mathbf{a}_{kr} + k_T \sin\theta_T \mathbf{a}_{ky} \\ \mathbf{k}_R = k_R \cos\theta_R \mathbf{a}_{kr} + k_R \sin\theta_R \mathbf{a}_{ky} \end{cases} \tag{4}$$

where $\mathbf{a}_{kr}$ and $\mathbf{a}_{ky}$ are downrange and cross-range unit vector, respectively. k_T and k_R are the absolute values of $\mathbf{k}_T$ and $\mathbf{k}_R$, respectively.

Based on the principle of electromagnetic wave propagation, we know that

$$\mathbf{k}_V = \mathbf{k}_T + \mathbf{k}_R \tag{5}$$

In addition,

$$k_T = k_R = 2\pi f/c \triangleq k \tag{6}$$

where k represents the wavenumber corresponding to the operating frequency. According to (4), (5) and (6), the downrange and cross-

range components of the virtual element wavenumber can be calculated as follows:

$$\begin{cases} k_r = k(\cos\theta_T + \cos\theta_R) \\ k_y = k(\sin\theta_T + \sin\theta_R) \end{cases} \tag{7}$$

Substituting (6) into (7), the operating frequency which is the function of k_r and k_y can be expressed as follows:

$$f(k_r, k_y) = \frac{c\sqrt{k_r^2 + k_y^2}}{4\pi\cos[\theta_T - \arctan(k_r/k_y)]} \tag{8}$$

If the radar image of the mth SIMO $I_m\,(r,\, y)$ is implemented with the 2-D fast Fourier transform (FFT), we can obtain the ROS. We denote the ROS of the left part array and the right part array as Ω_L and Ω_R, respectively. ROS of a SIMO array is the combination of Ω_L and Ω_R. Moreover, the boundary of Ω_L and Ω_R including the frequency boundary can be determined according to (7) and (8) as well as the imaging geometry. It will be used to calculate the AR in the image-domain. Fig. 6 provides a more detailed description about the boundary of the ROS. The red and blue colors are used to denote the left part array and the right part array, respectively.

4.3. Calculation of AR

Before we calculate AR in the image-domain, we determine the boundary of Ω_L and Ω_R as follows:

$$\begin{cases} \Omega_L = \{\Omega(k_r, k_y),\ \theta(k_r, k_y) \in (\theta_T, \theta_1),\ f(k_r, k_y) \in (f_L, f_H)\} \\ \Omega_R = \{\Omega(k_r, k_y),\ \theta(k_r, k_y) \in (\theta_2, \theta_T),\ f(k_r, k_y) \in (f_L, f_H)\} \end{cases} \tag{9}$$

where $\theta(k_r,\, k_y) \triangleq \arctan(k_y/k_r)$. $\theta_1(k_r,\, k_y)$ and $\theta_2(k_r,\, k_y)$ shown in Fig. 6(d) are computed as:

$$\tan\theta_1 = \frac{\sin\theta_T + \sin\theta_R^1}{\cos\theta_T + \cos\theta_R^1} \tag{10}$$

$$\tan\theta_2 = \frac{\sin\theta_T + \sin\theta_R^N}{\cos\theta_T + \cos\theta_R^N} \tag{11}$$

Using the above results, AR can be computed in the image-domain as follows:

$$\begin{aligned} \rho(\theta_P; \theta_T) &= \frac{1}{M}\sum_{m=1}^{M} \rho_m(\theta_P; \theta_T) = \frac{1}{M}\sum_{m=1}^{M} \frac{A_L^m}{A_R^m} \\ &= \frac{1}{M}\sum_{m=1}^{M} \frac{\int_{\Omega_L} |G_m(k_r, k_y)|\, dk_r dk_y}{\int_{\Omega_R} |G_m(k_r, k_y)|\, dk_r dk_y} \end{aligned} \tag{12}$$

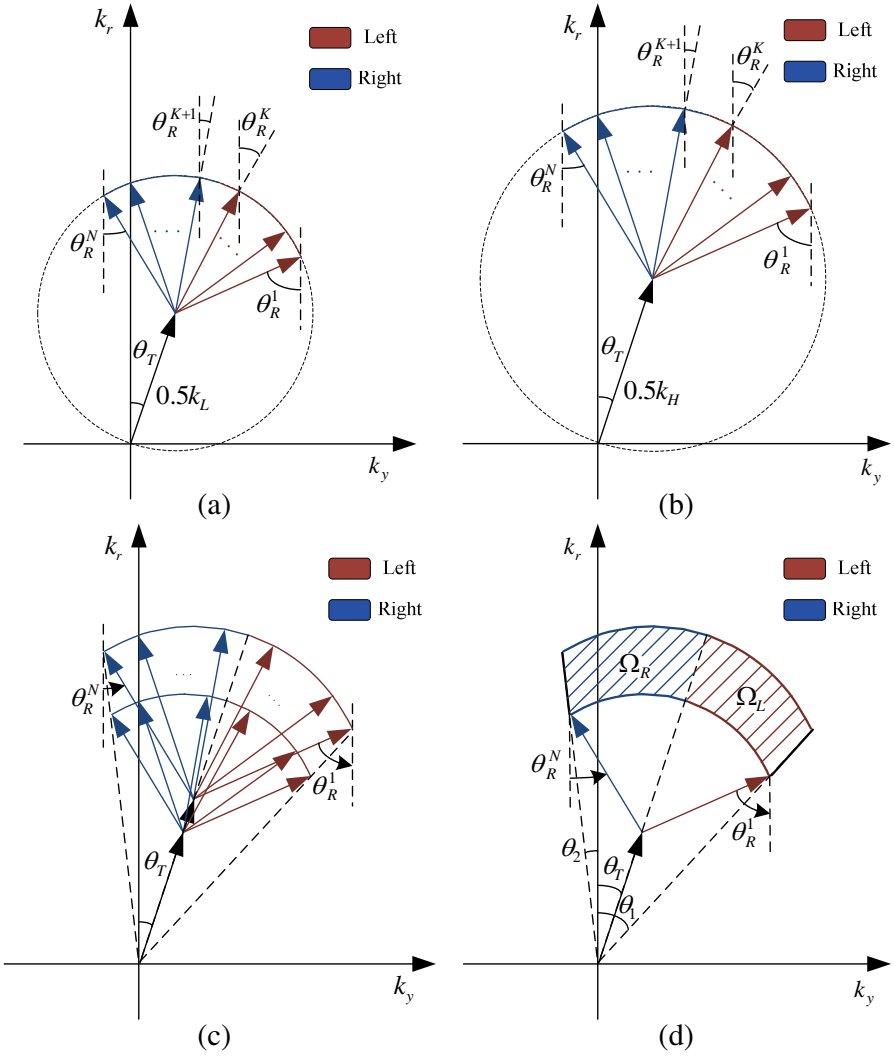

Figure 6. ROS of a SIMO array. (a) ROS of the single-frequency signal with frequency being the minimum frequency f_L (or $k_L = 2\pi f_L/c$), (b) ROS of the single-frequency signal with frequency being the maximum frequency f_H (or $k_H = 2\pi f_H/c$), (c) ROS of the wideband signal with the operating frequency from f_L to f_H, (d) ROS of the left part array and the right part array.

where $G_m(k_r, k_y)$ is the 2-D Fourier transform of $I_m(r, y)$ with respect to r and y. $\rho_m(\theta_P; \theta_T)$ and $\rho(\theta_P; \theta_T)$ are the AR calculated from the mth SIMO array and MIMO array, respectively. $\rho(\theta_P; \theta_T)$ is the averaging result of $\rho_m(\theta_P; \theta_T)$. A_L^m and A_R^m are the echo intensity of the left part and right part accumulated from the mth SIMO array, respectively. Thus, using (7)–(12), we can calculate AR in the image-domain directly. Dichotomy algorithm [33] could be used to speed up in estimating the pose angle based on the calculated AR.

5. EXPERIMENTAL RESULT

5.1. Experimental System Description

We conduct the experiments in an anechoic chamber using a radio frequency (RF) measurement system. This newly-integrated RF system consists of a network analyzer (Model Agilent N5242A) which transmits a stepped frequency waveform, RF cables, antennas, 3-D antenna positioning system, and computer controller. The working frequency of the transmitting and receiving antenna ranges from 2 GHz to 4 GHz with 1001 frequency points. Two horn antennas are used as transmitter and receiver.

Figure 7 shows the MIMO data collection scenario with $M = 3$. Both the optical photo of the radar system and experimental scene layout are provided, where the U-shape structure in Fig. 7 consists of three cinder brick walls. In the experiment, the transmitting antenna is placed at three different positions (0, 0.8 m), (0, 1.8 m) and (0, 2.8 m), respectively. The receiving antenna is fixed on a platform moving along the y-direction to form a linear receiving array from 0.9 m to 2.7 m with 0.05 m interval. Therefore, in this way, a MIMO array data can be obtained equivalently with $M = 3$ and $N = 37$.

The pose angles of the left wall-wall-floor trihedral $\theta_P^L = -31^\circ$

(a) (b) (c)

Figure 7. MIMO radar experimental setup with different transmitting locations. (a) $y = 0.8$ m, (b) $y = 1.8$ m, (c) $y = 2.8$ m.

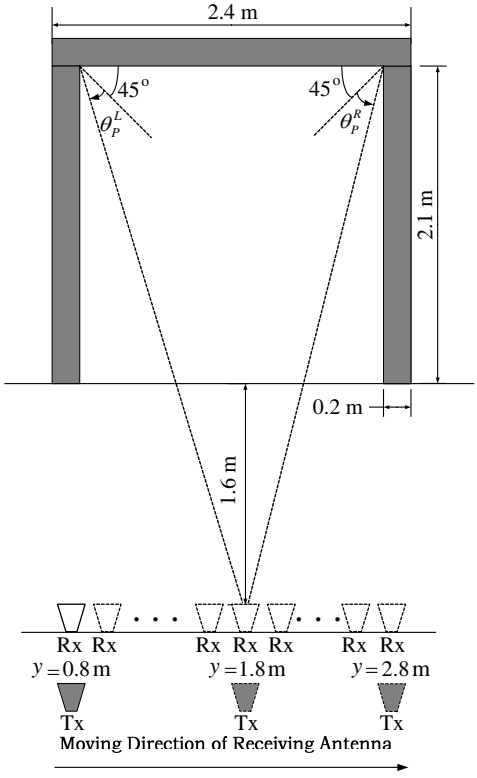

Figure 8. Experimental scene layout.

and the right wall-wall-floor trihedral $\theta_P^R = 28°$ are depicted in Fig. 8, which are defined according to the center of the receiver array.

5.2. Experimental Results

Figure 9 shows the BP imaging results of the U-shape wall with the transmitting antenna at three positions.

Figure 9 clearly shows the left trihedral, right trihedral and back wall plate. The left and right wall-wall-floor trihedra are very weak when the transmitter is located at (0, 0.8 m) and (0, 2.8 m), respectively. If the whole aperture is divided into a set of subapertures, it should be noted that for dihedra and plates, most or all of the scattering energy is concentrated in a single or a little more subaptures, while for trihedra, the scattering center may persist across multiple subapertures. As a result, the radar images are assumed to be segmented to isolate trihedra and plate primitives. One way to do

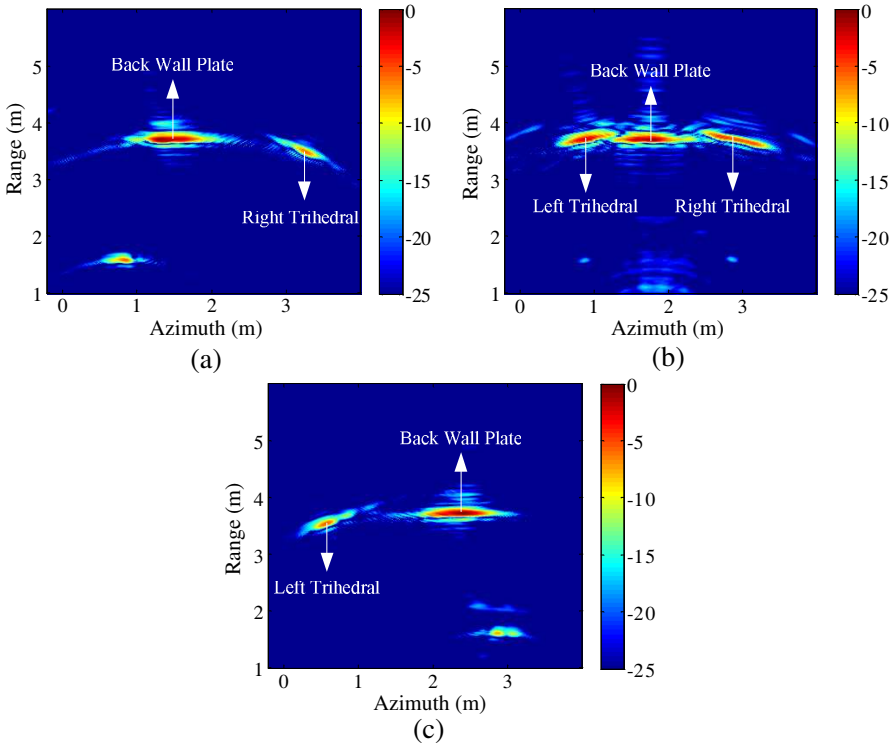

Figure 9. Radar image of the U-shape wall with different transmitting locations. (a) $y = 0.8\,\mathrm{m}$, (b) $y = 1.8\,\mathrm{m}$, (c) $y = 2.8\,\mathrm{m}$.

so is to separately treat cardinal-angle subaperture images and off-cardinal-angle subaperture images, with the assumption that returns from the buildings on cardinal angles are dominated by returns from plates and dihedra, while returns from buildings off cardinal angles are dominated by trihedra [34]. By using this method, we are able to extract the ROI of the left and the right wall-wall-floor trihedral.

We take the transmitting antenna at $(0, 1.8\,\mathrm{m})$ for example. Fig. 10(a) presents the 2-D FFT results of the left trihedral ROI, and Fig. 10(b) presents the right case. The ROS of the left part array Ω_L and the right part array Ω_R for each trihedral is also indicated in Fig. 10.

As we have got the ROS of the two trihedra in the U-shape wall scene, AR can be calculated in the wavenumber domain according to (12). We choose the pose angle whose corresponding AR is closer to the experimental result as the estimation value. As a result, dichotomy

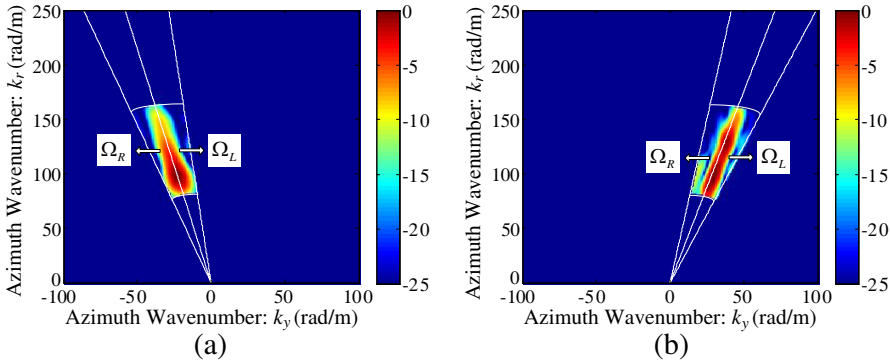

Figure 10. ROS and the corresponding boundary of the trihedrals, $y = 1.8$ m. (a) ROS of left wall-wall-floor trihedral, (b) ROS of right wall-wall-floor trihedral.

Table 1. Pose angle estimation results.

Trihedral	$\rho(\theta_P; \theta_T)$	Estimated Pose Angle
Left Wall-Wall-Floor	0.8024	$-26°$
Right Wall-Wall-Floor	1.3238	$29°$

algorithm could be used to speed up the estimation procedure. The real pose angle is obtained according to the imaging geometry. Table 1 presents the final results.

The final estimated pose angles listed in Table 1 have proved not only their good accordance with the real pose angles but also the effectiveness of our proposed method. Comparing with the true value of the pose angles, the influence of the estimation error whose maximum absolute value is $5°$ on mapping the interior structure of a building could be neglected.

6. CONCLUSIONS

Building layout mapping is an emerging research field in TWRI. Pose angle information of principal scatterers especially trihedral can improve the accuracy of building layout estimation. In this paper, we have proposed a pose angle estimation method in the image domain. When radar operates with a MIMO array, we analyze the virtual aperture imaging model in the wavenumber domain and propose AR to measure the pose angle difference. The field experimental results in Section 5 not only show that the parametric model accurately describe

the dominant response of trihedral, but also proves that the proposed method works well in estimating the pose angle. It is hoped that based on the preliminary results in this paper, we are able to predict the building interior structure in TWRI using the parametric model and the proposed image-domain method.

ACKNOWLEDGMENT

This work was supported by the National Natural Science Foundation of China under Grants 61271441 and 61201329, the Foundation for the Author of National Excellent Doctoral Dissertation of China under Grant 201046, the Program for New Century Excellent Talents in University under Grant NCET-10-0895, the research project of NUDT under Grant CJ12-04-02.

REFERENCES

1. Amin, M. G., *Through-the-wall Radar Imaging*, CRC Press, Boca Raton, FL, 2011.
2. Borek, S. E., "An overview of through the wall surveillance for homeland security," *Proceedings of the 34th Applied Imagery and Pattern Recognition Workshop (AIPR05)*, 6, 2005.
3. Baranoski, E. J., "Through wall imaging: Historical perspective and future directions," *IEEE International Conference on Acoustics, Speech and Signal Processing, ICASSP*, 5173–5176, 2008.
4. Jia, Y., L. Kong, X. Yang, and Z. Ao, "Target detection in multi-channel through-wall-radar imaging," *IEEE Radar Conference (RADAR)*, 0539–0542, 2012.
5. Dogaru, T., A. Sullivan, C. Kenyon, and C. Le, "Radar signature prediction for sensing-through-the-wall by Xpatch and AFDTD," *DoD High Performance Computing Modernization Program Users Group Conference*, 339–343, 2009.
6. Debes, C., M. G. Amin, and A. M. Zoubir, "Optimal decision fusion in through-the-wall radar imaging," *2009 IEEE/SP 15th Workshop on Statistical Signal Processing*, 761–764, 2009.
7. Jia, Y., L. J. Kong, and X. B. Yang, "A novel approach to target localization through unknown walls for through-the-wall radar imaging," *Progress In Electromagnetics Research*, Vol. 119, 107–132, 2011.
8. Verma, P. K., A. N. Gaikwad, D. Singh, and M. J. Nigam, "Analysis of clutter reduction techniques for through wall imaging

in UWB range," *Progress In Electromagnetics Research B*, Vol. 17, 29–48, 2009.

9. Zheng, W., Z. Zhao, and Z.-P. Nie, "Application of TRM in the UWB through wall radar," *Progress In Electromagnetics Research*, Vol. 87, 279–296, 2008.
10. Narayanan, R. M., M. C. Shastry, P.-H. Chen, and M. Levi, "Through-the-wall detection of stationary human targets using Doppler radar," *Progress In Electromagnetics Research B*, Vol. 20, 147–166, 2010.
11. Davy, M., T. Lepetit, J. de Rosny, C. Prada, and M. Fink, "Detection and imaging of human beings behind a wall using the dort method," *Progress In Electromagnetics Research*, Vol. 110, 353–369, 2010.
12. Ram, S. S. and H. Ling, "Through-wall tracking of human movers using joint Doppler and array processing," *IEEE Geosci. Remote Sens. Lett.*, Vol. 5, No. 3, 537–541, 2008.
13. Li, Y., X. Jing, H. Lv, and J. Wang, "Analysis of characteristics of two close stationary human targets detected by impulse radio UWB radar," *Progress In Electromagnetics Research*, Vol. 126, 429–447, 2012.
14. Riaz, M. M. and A. Ghafoor, "Principle component analysis and fuzzy logic based through wall image enhancement," *Progress In Electromagnetics Research*, Vol. 127, 461–478, 2012.
15. Zhang, W. and A. Hoorfar, "Two-dimentional diffraction tomographic algorithm for through-the-wall radar imaging," *Progress In Electromagnetics Research B*, Vol. 31, 205–218, 2011.
16. De Wit, J. J. M., W. L. van Rossum, and F. M. A. Smits, "SAPPHIRE-a novel building mapping radar," *Proceedings of the 39th European Microwave Conference*, 1896–1899, 2009.
17. Smits, F. M. A., J. J. M. de Wit, W. L. van Rossum, A. P. M. Maas, R. J. Bolt, and C. M. Lievers, "3D mapping of buildings with SAPPHIRE," *6th EMRS DTC Technical Conference*, 1–7, 2009.
18. De Wit, J. J. M., W. L. van Rossum, and F. M. A. Smits, "Principal scatterer detection in buildings with SAPPHIRE," *2010 8th European Conference on Synthetic Aperture Radar (EUSAR)*, 921–924, 2010.
19. Le, C., T. Dogaru, L. H. Nguyen, and M. A. Ressler, "Ultrawideband (UWB) radar imaging of building interior: Measurements and predictions," *IEEE Trans. on Geosci. Remote Sens.*, Vol. 47, No. 5, 1409–1420, 2009.

20. Gerry, M. J., L. C. Potter, I. J. Gupta, and A. van der Merwe, "A parametric model for synthetic aperture radar measurements," *IEEE Trans. on Antennas and Propag.*, Vol. 47, No. 7, 1179–1188, 1999.
21. Xu, M., S. Xiao, and X. Wang, "Radar target's space-frequency instantaneous polarization characteristics and its application on geometrical structure retrieval," *Journal of Electronics & Information Technology*, Vol. 31, No. 5, 1127–1131, 2009.
22. Dilsavor, R., W. Ailes, P. Rush, F. Ahmad, W. Keichel, G. Titi, and M. Amin, "Experiments on wideband through the wall imaging," *Proceedings of SPIE*, 196–209, 2005.
23. Dogaru, T., C. Le, and L. Nguyen, "SAR images of a simple room based on computer models," US Army Research Laboratory, ARL, Adelphi, 2010.
24. Savelyev, T. G., X. Zhuge, A. G. Yarovoy, L. P. Ligthart, J. M. Lerat, L. Duchesne, and J. Fortuny-Guasch, "Development of through-wall imaging radar with planar MIMO array," *Proceedings of the 8th European Radar Conference*, 226–229, 2011.
25. Oaknin, J., R. Daisy, and A. Beeri, "Antenna array design for 'through wall imaging' systems by means of information maximization," *Proc. of SPIE*, 69470F1–69470F7, 2008.
26. Chen, H.-W., J. Ding, X. Li, and Z. Zhuang, "MIMO radar systems design based on maximum channel capacity," *Progress In Electromagnetics Research B*, Vol. 34, 313–326, 2011.
27. Hatam, M., A. Sheikhi, and M. A. Masnadi-Shirazi, "Target detection in pulse-train MIMO radars applying ICA algorithms," *Progress In Electromagnetics Research*, Vol. 122, 413–435, 2012.
28. Zhou, W., J.-T. Wang, H. W. Chen, and X. Li, "Signal model and moving target detection based on MIMO synthetic aperture radar," *Progress In Electromagnetics Research*, Vol. 131, 311–329, 2012.
29. McCorkle, J. W., "Focusing of synthetic aperture ultra wideband data," *IEEE International Conference of Systems Engineering*, 1–5, 1991.
30. Subotic, N., E. Keydel, J. Burns, A. Morgan, K. Cooper, B. Thelen, B. Wilson, W. Williams, S. McCarty, B. Lampe, B. Mosher, and D. Setterdahl, "Parametric reconstruction of internal building structures via canonical scattering mechanisms," *IEEE International Conference on Acoustics, Speech and Signal Processing, ICASSP*, 5189–5192, 2008.
31. Jackson, J. A., B. D. Rigling, and R. L. Moses, "Parametric

scattering models for bistatic synthetic aperture radar," *IEEE Radar Conference*, 1–5, 2008.

32. Jin, T., J. Lou, and Z. Zhou, "Extraction of landmine features using a forward-looking ground penetrating radar with MIMO array," *IEEE Trans. on Geosci. Remote Sens.*, Vol. 50, No. 10, 4135–4144, 2012.
33. Jiang, L., "Ordinary dichotomy and global linearization," *Nonlinear Analysis Theory, Methods & Applications*, Vol. 70, 2722–2730, 2009.
34. Ertin, E. and R. L. Moses, "Through-the-wall sar attributed scattering center feature estimation," *IEEE Trans. on Geosci. Remote Sens.*, Vol. 47, No. 5, 1338–1348, 2009.